

Article

Finite Element Analysis of Axially Loaded RC Walls with Openings Strengthened Using Textile Reinforced Mortar for Sustainable Structures

Mohannad Alhusban and Azadeh Parvin *

Department of Civil and Environmental Engineering, The University of Toledo, Toledo, OH 43606, USA

* Correspondence: azadeh.parvin@utoledo.edu

Abstract: Sustainable solutions in the building construction industry promotes the use of innovative materials such as textile reinforced mortar (TRM) as a strengthening technique resulting in a reduced life-cycle cost. This paper presents a nonlinear finite element analysis (FEA) of TRM strengthened RC walls with cut-out openings under axial loading. FEA models were developed and validated with two experimental tests from the literature. Subsequently, a parametric study was performed to investigate the contribution of TRM in strengthening RC walls considering various opening sizes, types, numbers and orientations of window openings, and TRM strengthening configurations. The parametric study results revealed that strengthened models with smaller opening sizes had higher axial strength enhancement. Furthermore, the increase in the axial load capacities of walls with door and window openings were 34 and 26%, respectively, as compared to the corresponding control ones. TRM was more effective with a lower opening aspect ratio (H_o/L_o). In addition, confining the wall piers with U-shaped TRM jackets was the most effective configuration in improving the walls' axial strengths with maximum enhancements of 16 and 22% as compared to the models strengthened with side-bonded sheets and strips, respectively. Finally, the axial strengths of the FEA models were also compared with the existing empirical solution and showed reasonable correlation with an average discrepancy of 15%.

Keywords: reinforced concrete; walls; cut-out openings; textile-reinforced mortar; TRM; finite element analysis; axial load; ANSYS



Citation: Alhusban, M.; Parvin, A. Finite Element Analysis of Axially Loaded RC Walls with Openings Strengthened Using Textile Reinforced Mortar for Sustainable Structures. *Buildings* **2022**, *12*, 1993. <https://doi.org/10.3390/buildings12111993>

Academic Editors: Junbo Sun, Nina Liu, Debo Zhao and Genbao Zhang

Received: 15 October 2022

Accepted: 11 November 2022

Published: 16 November 2022

Publisher's Note: MDPI stays neutral with regard to jurisdictional claims in published maps and institutional affiliations.



Copyright: © 2022 by the authors. Licensee MDPI, Basel, Switzerland. This article is an open access article distributed under the terms and conditions of the Creative Commons Attribution (CC BY) license (<https://creativecommons.org/licenses/by/4.0/>).

1. Introduction

Reinforced concrete walls have become an important load-bearing structural element in the construction of buildings due to their essential advantages, such as cost-effectiveness and fast construction. Generally, RC walls are subjected to in-plane loads (axial and shear forces) and/or out-of-plane loads (wind). The in-plane axial loads are usually eccentric due to construction defects, corbel elements attached to the wall, and unequal load distribution on top of the wall resulting in out-of-plane deformation. On the other hand, axially loaded walls can be restrained in two, three, or four sides depending on the types of structure. RC walls supported at the top and bottom only, behave with one-way action (OW), described by uniaxial curvature parallel to the direction of the load, usually seen in tilt-up concrete structures. Furthermore, axially loaded walls can operate with two-way action (TW) when restrained at three or four sides and are often encountered in high rise buildings. These walls deflect in both horizontal and vertical directions.

Existing buildings may need a modification in the functional requirements of the structural elements, such as creating new openings for doors, windows, or heating systems in existing RC walls. These types of openings are called cutout openings. Openings are often avoided to reduce the impact of discontinuous regions where high stresses are expected to occur. It also weakens the structure in terms of load-bearing capacity and reduces the stiffness of the walls. However, there has been a growing attention in modern

architectural designs to increase the living spaces or joining two adjacent rooms by creating new openings in existing RC walls. The behavior of RC walls with and without openings has been widely studied [1–4].

RC walls with cutout openings not only involve demolishing and repairing, but also require strengthening. The traditional ways of strengthening RC walls due to openings are either by concrete jacketing or constructing the RC frame next to the openings. These techniques have many drawbacks due to the use of additional concrete, such as high consumption of CO₂, longer service interruption, and redesigning the associated elements, such as columns and footings. Alternatively, walls can be externally strengthened by composites for sustainable structures due to the shorter construction time and lower life-cycle costs [5,6]. Fiber-reinforced polymer (FRP) attracted the most attention among all strengthening techniques due to its advantageous properties, such as high strength to weight ratio, ease of application, corrosion resistance, and fast construction [7]. Despite these advantages, FRP has some weaknesses due to the use of epoxy resin, such as high the cost of epoxy, its inapplicability on wet surfaces, and its low resistance to high temperatures. Therefore, a newer material, textile reinforced mortar (TRM), is a promising alternative to FRP in terms of sustainability and durability by substituting the epoxy with inorganic cementitious binders such as mortars in the strengthening of RC structures [8].

TRM is a composite comprised of textile fiber reinforcement (with open mesh geometry) combined with inorganic materials such as cementitious mortars. TRM is a sustainable, low-cost noncorrosive material, resistant to high temperatures, applicable on wet surfaces, and compatible with concrete and masonry substrates [9].

In the last decade, the interest in strengthening RC walls using externally bonded composites has increased. The use of FRP in strengthening pre-damaged RC walls with a cutout opening in one-way (OW) and two-way (TW) actions have been studied [10–12]. It was concluded that FRP could not fully restore the bearing capacity of the corresponding solid wall. However, as compared to the damaged walls with openings, FRP jacketing provided approximately 50% improvement in the axial load capacity [12].

On the other hand, the effectiveness of TRM composites have been widely explored for flexural and shear strengthening of RC beams and confinement of RC columns [13–17]. However, studies on the TRM strengthening of RC panels are extremely limited [18,19] and mostly focused on masonry-infill walls in RC frames [20–23]. Todut et al. [18] compared the effect of TRM strengthening with several FRP solutions in RC walls with openings subjected to in-plane shear. TRM strengthening improved the capacity of damaged panels with openings to their initial capacity. Recently, Sabau et al. [19] evaluated the capacity and stiffness improvements obtained by TRM in TW axially loaded RC wall panels with different opening sizes. TRM showed improvement of in- and out-of-plane rigidities of the RC walls. Furthermore, the failure mechanism was shifted from buckling of the reinforcement to concrete crushing.

From the reviewed literature above, there is an extreme lack of experimental as well as numerical investigations on TRM strengthening RC wall panels with cutout openings. In addition, there is a demand in the building construction industry on the use of sustainable solutions through the application of building materials with lower environmental impacts, such as TRM [24]. Furthermore, experimental testing is time-consuming and is not always available for large structural members. Hence, the need for comprehensive experimental studies can be replaced with complex numerical models validated with typical field tests. Comprehensive numerical simulations of RC walls with cutout openings using FEA are scarce.

The objective of the present study is to further investigate the TRM effectiveness on the axial and out-of-plane behavior of RC wall panels considering various crucial parameters not addressed before. Within this scope, the importance and relevance of key parameters related to the concrete and TRM were examined. Thus, the findings of this study deliver a set of data that is nonexistent on the performance of TRM-strengthened RC walls, which can be used to develop the design guidelines. In this paper, FEA models of TRM

strengthening RC walls with cutout openings under eccentric axial loading were developed and validated with two experimental studies from the literature [3,19]. Subsequently, a parametric study was performed on the validated models to examine the influence of various opening sizes (A_o/A_w ranged between 20% and 45%), types (doors and windows), numbers and orientations of windows, and strengthening configurations (U-shaped jackets and side-bonded strips applied around the openings) on the axial load capacity and failure modes of RC walls.

2. Description of Experimental Tests Adopted for Validation of FEA Models

Two experimental tests were selected to validate the accuracy of the developed finite element models of RC walls [3,19]. The two tests are identical except that the experiment carried out by Popescu et al. [3] was adopted to validate the control models while the one by Sabau et al. [19] was selected for the corresponding strengthened ones. The wall panels were designed as two-way walls (out-of-plane movement is restricted on all edges) and it was subjected to only eccentric axial load applied on the top edge. These boundary conditions generate out-of-plane bending in vertical and horizontal directions. The walls were strengthened with one-layer side-bonded TRM sheets applied on both faces to improve their axial and flexural capacities. Figure 1 shows the dimensions, reinforcement details, and boundary conditions of the control and strengthened walls [3,19]. The out-of-plane displacement was measured at point (P) for all control and strengthened walls.

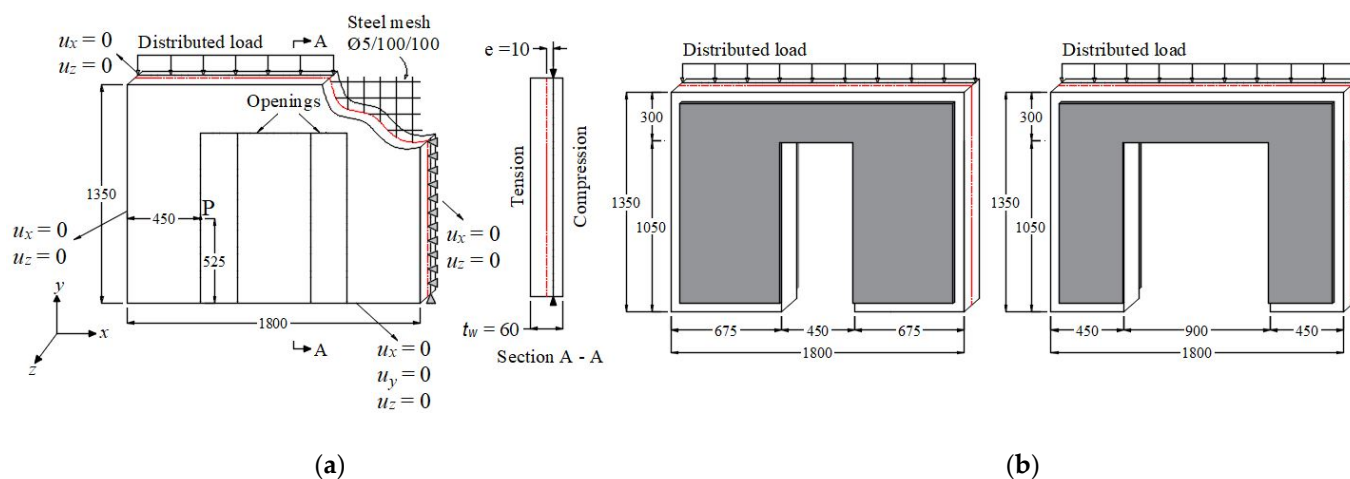


Figure 1. Dimensions, reinforcement details, and boundary conditions: (a) control walls according to Popescu et al. [3]; (b) TRM strengthened walls according to Sabau et al. [19]. (Unit: mm).

The concrete compressive strengths of $150 \times 150 \times 150$ mm cubes were 62.8 MPa and 68 MPa for the control and strengthened walls, respectively, while the yield and ultimate strengths of the steel mesh were 634 MPa and 693 MPa, respectively. The textile mesh material of the selected walls was carbon, with a tensile strength, modulus of elasticity, and an ultimate tensile strain of 4700 MPa, 240 GPa, and 1.8%, respectively [19]. The mortar had a compressive strength of 37.8 MPa and a flexural strength of 4.96 MPa.

The TRM strengthening procedure follows the typical lay-up method. Prior to the TRM application, the concrete surface needs to be prepared by creating grooves in the form of a grid. Then, the first layer of mortar is applied to the concrete surface by using a trowel. Thereafter, a layer of textile is installed and pressed slightly into the mortar. This procedure is repeated until the required number of textile sheets are installed (Figure 2). The bond between the textile and mortar is created by mechanical interlock, which is formed due to the mortar penetration through the textile mesh voids.

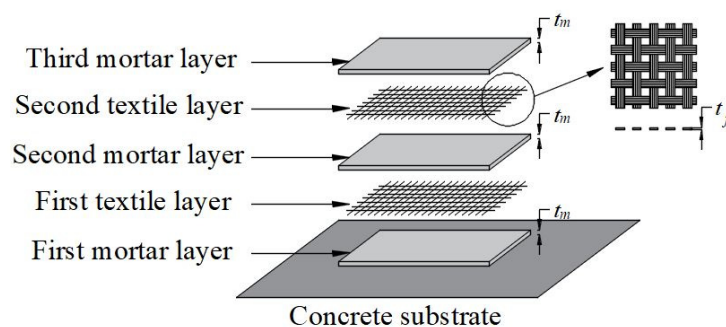


Figure 2. Schematic representation of typical TRM system.

3. Finite Element Analysis Modelling of RC and Retrofitted Walls

In this study, the nonlinear finite element modelling was performed using ANSYS (Mechanical APDL) program software. The details of the nonlinear finite element analysis procedure are described in the following sections.

3.1. Element Types

CPT215, a 3-D eight-node solid element supported by the microplane material models with the capability of elasticity, stress stiffening, and large strain and deformation was utilized to model the concrete. The steel reinforcement mesh was modelled using the REINF264 element in the form of a two-node 3-D uniaxial spar element with a capability of plasticity, large strain, and deformation. The steel plates at the load and support locations were modelled using the SOLID185 element. The mortar and the textile were modelled individually using two different elements with node-to-node connection assuming no slippage, which was the case in the experiment. For the textile mesh, the SHELL181 element was selected since this element is well-suited in modelling thin to moderate-thick structural elements [25]. The shell section associated with the SHELL181 element allows the use of multilayers with various thicknesses and orientations. SOLID65, an 8-node 3-D element with the capability of cracking and crushing, was used to model the mortar. Contact and target elements were considered to simulate the concrete–mortar interface.

3.2. Material Models

A regularized coupled damage–plasticity microplane model was adopted for the concrete [26,27]. In this model, the material behavior is simulated by utilizing uniaxial stress versus strain laws on multiple individual planes called microplanes. This approach was employed to capture the inelastic behavior of concrete and to overcome the numerical instability of the analysis due to the strain-softening of the material [28]. The coupled damage–plasticity microplane model can be defined by a smooth three-surface microplane Drucker–Prager with tension and compression cap surfaces (see Figure 3). The main advantage of implementing the two cap surfaces is to limit the expansion of the yield surface in both tension and compression.

The coupled damage–plasticity model requires 15 parameters to simulate elasticity, plasticity, damage, and solution regularization. The modulus of elasticity (E_c) and Poisson's ratio (ν) were assigned to model the elastic behavior of the concrete where the former was calculated using Equation (1) [29]:

$$E_c = 4700 \sqrt{f_{uc}} \quad (1)$$

where f_{uc} is the ultimate concrete compressive strength.

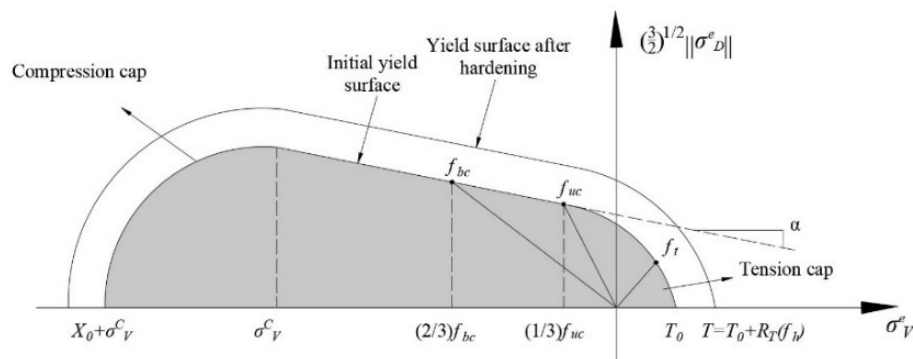


Figure 3. Smooth three-surface microplane cap yield function.

To model the plastic behavior of the concrete, the Drucker–Prager yield surface, the compression cap, and the hardening were identified. The strength parameters, namely the uniaxial compressive strength (f_{uc}), uniaxial tensile strength (f_{ut}), and biaxial compressive strength (f_{bc}) were employed to define the Drucker–Prager yield surface. The uniaxial compressive and tensile strengths were obtained from the experimental studies used for the validation, whereas the biaxial compressive strength (f_{bc}) was empirically approximated [30].

$$f_{bc} = 1.15 f_{uc} \tag{2}$$

The material constant (σ_v^c), which is the abscissa of the point where the compression cap and Drucker–Prager yield surface intersect, was used to determine the compression cap’s location. The constant σ_v^c represents the transition point from plastic volumetric expansion to plastic volumetric compaction. If no triaxial test results are available, the value of σ_v^c can be estimated using Equation (3).

$$\sigma_v^c \leq -2/3 f_{bc} \tag{3}$$

Thereafter, the parameter R , which represents the ratio of the major to minor axes of the compression cap, was assigned to determine the compression cap’s shape. The parameter R can be calculated as follows:

$$R = \frac{X_0}{f_1(\sigma_v^c)} \tag{4}$$

where X_0 is the length of the major axis of the cap along the volumetric stress axis (x -axis) and f_1 is the Drucker–Prager yield function.

The tension cap location and shape are determined by the intersection of the Drucker–Prager yield function with volumetric axis through parameters T_0 and T where the former represents the initial intersection of the cap, and the latter refer to the intersection point after hardening. The hardening function (f_h) is used to control the tension cap’s size. The tension cap parameters were not required as input for the definition of the microplane material and were calculated automatically by ANSYS.

The interaction of the hardening and damage variables limits the damage evolution and softening of the concrete. It is noted that these variables affect only the post-yielding plateau of the concrete stress versus strain curve, that is, after reaching the elastic limit. The values of these parameters can be obtained through cyclic testing. However, since no cyclic tests were available in the experimental study, the default values suggested by Zreid and Kaliske [28] and adopted by ANSYS for the hardening parameter (D), tension cap hardening factor (R_T), compression damage evolution constant (β_c), and threshold (γ_{c0}) were assumed. The tension damage threshold (γ_{t0}) was taken equal to zero assuming the

softening of the concrete in tension starts once the elastic limit is reached [28]. In addition, the tension damage evolution parameter (β_t) was calculated using Equation (5).

$$\beta_t = 1.5 \beta_c \quad (5)$$

To mitigate the numerical instability of the solution due to the strain-softening of the material, the nonlocal implicit gradient regularization method was adopted by adding two extra degrees of freedom for each node. In this method, two parameters, namely the over-nonlocal (m) and nonlocal interaction range (c), were defined. The over-nonlocal parameter (m) is a numerical parameter that, with any value greater than 1, regularizes the solution and provides a mesh-independent convergence behavior. The typical value of the parameter (m) is 2.5. On the other hand, the interaction range parameter (c) controls the nonlocal interaction damage parameters and can be estimated using Equation (6):

$$c \geq 4l^2 \quad (6)$$

where l is the maximum element length [25]. It is noted that the accuracy of the results is still affected by the FE model mesh size. To calibrate the abovementioned parameters, a simple model of a cube with a side length of 150 mm was developed in ANSYS to construct the stress versus strain diagram of the material model used. This curve was then compared with existing analytical solutions [31,32]. Good calibration was achieved as shown in Figure 4a. All parameter values are shown in Table 1.

Table 1. Coupled damage–plasticity microplane model parameters.

Parameter Type	Parameter Subtype	Parameter Description	Parameter	Unit	Value
Elasticity	-	Young's modulus	E_c	MPa	34,538
	-	Poisson's ratio	ν	-	0.2
Plasticity	Drucker–Prager yield function	Uniaxial compressive strength	f_{uc}	MPa	54
		Biaxial compressive strength	f_{bc}	MPa	62.1
		Uniaxial tensile strength	f_{ut}	MPa	4.6
	Hardening	Tension cap hardening factor	R_t	-	1
		Hardening parameter	D	MPa	40,000
	Compression cap	Compression cap location	σ_{vc}	MPa	-41.4
Compression cap shape		R	-	2	
Damage	-	Threshold for tension damage	γ_{t0}	-	0
	-	Threshold for compression damage	γ_{c0}	-	2.0×10^{-5}
	-	Tension damage parameter	β_t	-	3000
	-	Compression damage parameter	β_c	-	2000
Nonlocal	-	Nonlocal interaction range parameter	c	mm ²	1600
	-	Over nonlocal parameter	m	-	2.5

A bilinear elastic–perfectly plastic stress versus strain curve for the steel mesh was assumed (see Figure 4b). On the other hand, a linear elastic behavior was assigned for the steel plates. The moduli of elasticity E and Poisson's ratios (γ) for the steel mesh and plates were 200 GPa and 0.3, respectively. The yield and ultimate strengths of the steel reinforcement were 634 MPa and 693 MPa, respectively.

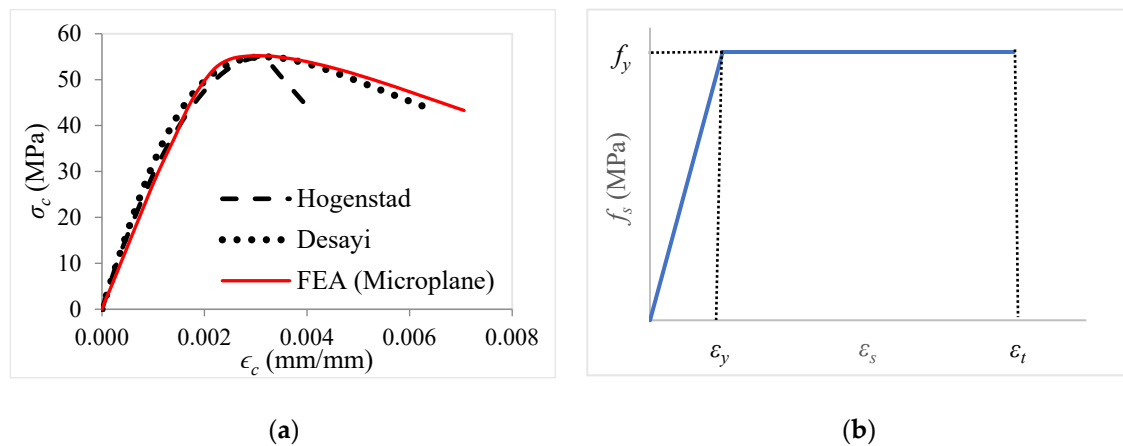


Figure 4. Stress versus strain curves: (a) concrete; (b) steel reinforcements.

The textile has linear orthotropic behavior in which the mechanical properties are identical along the fiber's direction in the textile's plane and different in the out-of-plane direction. Since two different elements were used to simulate the mortar and the textile, the orthotropic behavior assumption for the textile guarantees equal strength and stiffness along the two directions in the plane of the textile. Two local coordinate systems were specified in the modelling for each side of the wall following the right-hand rule in which the local x - and y -axes were parallel to the textile plane, while the z -axis was perpendicular.

The required parameters for the carbon textile modelling were the moduli of longitudinal elasticity (E_x , E_y , and E_z), moduli of transversal elasticity (G_{xy} , G_{yz} , and G_{xz}) and Poisson's ratios (ν_{xy} , ν_{yz} , and ν_{xz}). Based on the values used in the experiment of the carbon textile, the moduli of longitudinal elasticity were 240, 30, and 30 GPa in x , y , and z directions, respectively. The Poisson's ratios were assumed equal to 0.22, 0.22, and 0.3 for ν_{xy} , ν_{xz} , and ν_{yz} , respectively [33]. The moduli of transversal elasticity, G_{xy} , G_{xz} , and G_{yz} , were obtained using Equations (7) and (8), resulting in 13.2, 13.2, and 8.3 Gpa, respectively.

$$G_{xz} = G_{xy} = \frac{E_x E_y}{(E_x + E_y) + 2(\nu_{xy} E_x)} \quad (7)$$

$$G_{yz} = \frac{E_z}{2(1 + \nu_{xz})} \quad (8)$$

The bond characteristics at the TRM–concrete interface is affected by various parameters, such as the effective bond length, number of layers, and fiber material. The three common failure modes related to the externally bonded TRM are the detachment of jacket from the concrete, slippage of fibers within the matrix, and rupture of the fibers. Although no sign of debonding was observed in the experiment, detachment of the TRM jackets were considered in the modelling.

Younis and Ebead [34] proposed analytical models to predict the bond capacity at the TRM–concrete interface. A linear behavior between the tangential contact stress and slip of the TRM was noticed up to the maximum tangential contact stress. Beyond that point, a significant increase in the slip value was observed. Thus, the cohesive zone material model (CZM) with bilinear behavior was assumed to model the bond behavior at the TRM–concrete interface. Five parameters were needed to simulate the debonding of the jackets, namely the maximum normal contact stress (σ_{max}), the maximum equivalent tangential contact stress (τ_{max}), the critical fracture energies for normal separation (G_{cn}) and tangential slip (G_{ct}), and the artificial damping coefficient (η).

The maximum normal contact stress (σ_{max}) was assumed equal to the concrete tensile strength (f_t) [35]. The following equation was used to obtain the maximum equivalent tangential contact stress (τ_{max}) [34]:

$$\tau_{max} = 0.107\beta_L \sqrt{\frac{E_{TRM}\sqrt{f_m}}{t_{TRM}}} \quad (9)$$

where β_L is the bond length factor, E_{TRM} is the modulus of longitudinal elasticity of the TRM, f_m is the compressive strength of the mortar, and t_{TRM} is the thickness of the TRM jacket and taken equal to 8 mm [19]. A value of 1 was assigned for the bond length factor assuming that the effective and available bond lengths are equal since the application of the TRM was over the whole area of the walls' sides [34,36].

The critical fracture energies G_{cn} and G_{ct} were calculated according to Equations (10) and (11) as follows:

$$G_{cn} = G_{fo} \left(\frac{f'_c}{10} \right)^{0.7} \quad (10)$$

$$G_{ct} = 0.308\beta_w^2 \sqrt{f_t} \quad (11)$$

$$\beta_w = \sqrt{\frac{2 - b_f/b_c}{1 + b_f/b_c}} \quad (12)$$

where G_{fo} is the base critical fracture energy calculated based on the maximum aggregate size in the concrete, β_w is the width ratio factor obtained by Equation (12), and b_f and b_c are the widths of the TRM sheets and the concrete, respectively.

To overcome convergence issues and ensure that the maximum shear stresses do not exceed the maximum traction contact stress (τ_{max}), the artificial damping coefficient (η), which has time units, should be smaller than the minimum time-step size [25]. Thus, the coefficient (η) was taken equal to 0.05.

3.3. Mesh Generation and Boundary Conditions

Based on a preliminary mesh-sensitivity study, the largest element size was taken equal to 20 mm with an aspect ratio of approximately one (Figure 5). The element size selection aimed to achieve a balance between the result's accuracy and analysis time cost. The FE mesh with an element side length smaller than 20 mm had insignificant influence on the axial load values, as shown in Figure 5. Therefore, an element size of 20 mm was selected. The developed finite element models, boundary conditions, and reinforcement details of the TRM-strengthened RC walls with openings are shown in Figure 6a,b. Due to the symmetry of the vertical axis (y -axis), half of the wall was modelled to reduce the analysis time. The nodes at the plane of symmetry were constrained in the perpendicular direction to the y - z plane by assigning roller supports. The out-of-plane displacement was restrained on all edges simulating two-way (TW) RC walls, with rotations permitted at the top and bottom faces (pin support). An eccentricity of 10 mm (corresponds to $1/6 t_w$) was provided along the thickness of the walls at the top and bottom steel plates.

Large displacement static analysis was performed to account for the geometric non-linearities. A displacement-controlled analysis was performed by applying a vertical displacement on the nodes of the top plate to simulate the axial force in the experiment. The displacement was applied gradually and was divided into load steps and sub-steps. The full unsymmetric Newton–Raphson approach was used to update the stiffness of the model at each load iteration. Automatic time stepping was activated to control the load-step size and to obtain convergence of the solution. The default convergence criteria, which were based on force and displacement with tolerance limits of 0.5% and 0.1%, respectively, were used in this study.

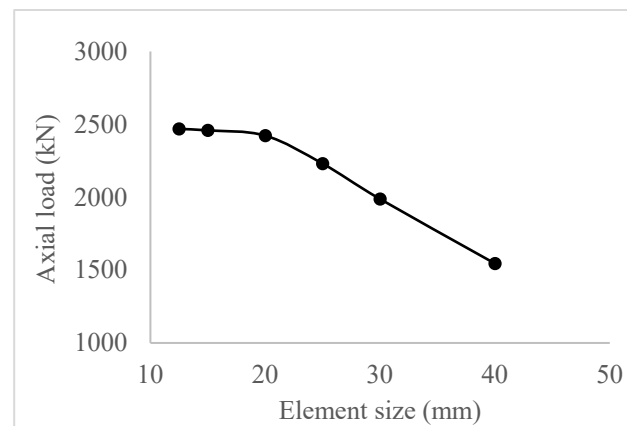


Figure 5. Mesh sensitivity analysis results.

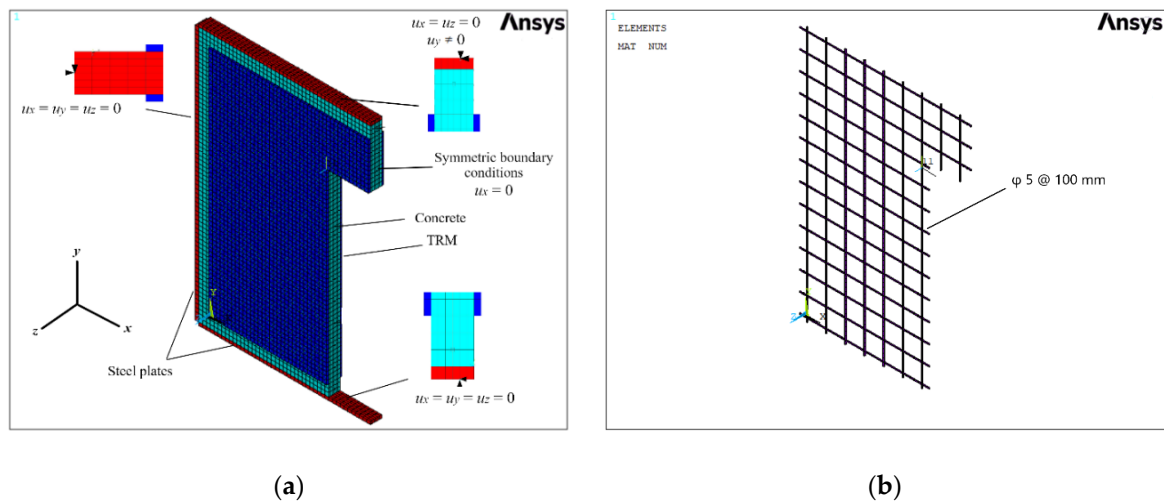


Figure 6. (a) Geometry and boundary conditions of the FEA models; (b) reinforcement details.

4. Validated Wall Model Results

To approve the accuracy of the FEA results, five models (three control and two TRM-strengthened) were developed and validated with the test results from the literature [3,19]. The test specimens and FEA wall model results are shown in Table 2. The FEA models are identified as follows: C and S refer to control and strengthened walls, respectively, N stands for no opening and D for door opening, and the last number refers to the ratio of the opening area with respect to the area of the wall. The experimental and FEA ultimate axial load and corresponding out-of-plane displacement, measured at point P as shown in Figure 1, were in good agreement with less than 10% difference.

Table 2. Results of the experiment and FEA models.

Experiment ID	FEA ID	Ultimate Load (kN)			Out-of-Plane Displacement (mm)		
		Experiment	FEA	Difference (%)	Experiment	FEA	Difference (%)
I-C	CN-0	2363	2423	2.5	16.4	15.5	5.5
I-S	CD-20	1500	1464	2.4	22.6	20.7	8.4
I-L	CD-39	1180	1128	4.4	9.6	9.1	5.2
SO1	SD-20	2130	1967	7.7	7.6	8.2	8.2
LO1	SD-39	1330	1345	1.1	5.8	5.3	8.6

Figure 7 shows the axial load versus out-of-plane displacement of the FEA models and test specimens. The load versus out-of-plane displacement curves of the developed models agrees well with the experimental ones. For the solid wall, the experimental specimen had higher stiffness as compared to the model CN-0 due to settlement of the test setup, which resulted in small out-of-plane displacement at initial loads [3]. However, both walls showed better correlation at higher loads. Similar observations were made for the control walls with small openings. On the other hand, the FEA models with large openings were slightly stiffer as compared to the corresponding tested walls.

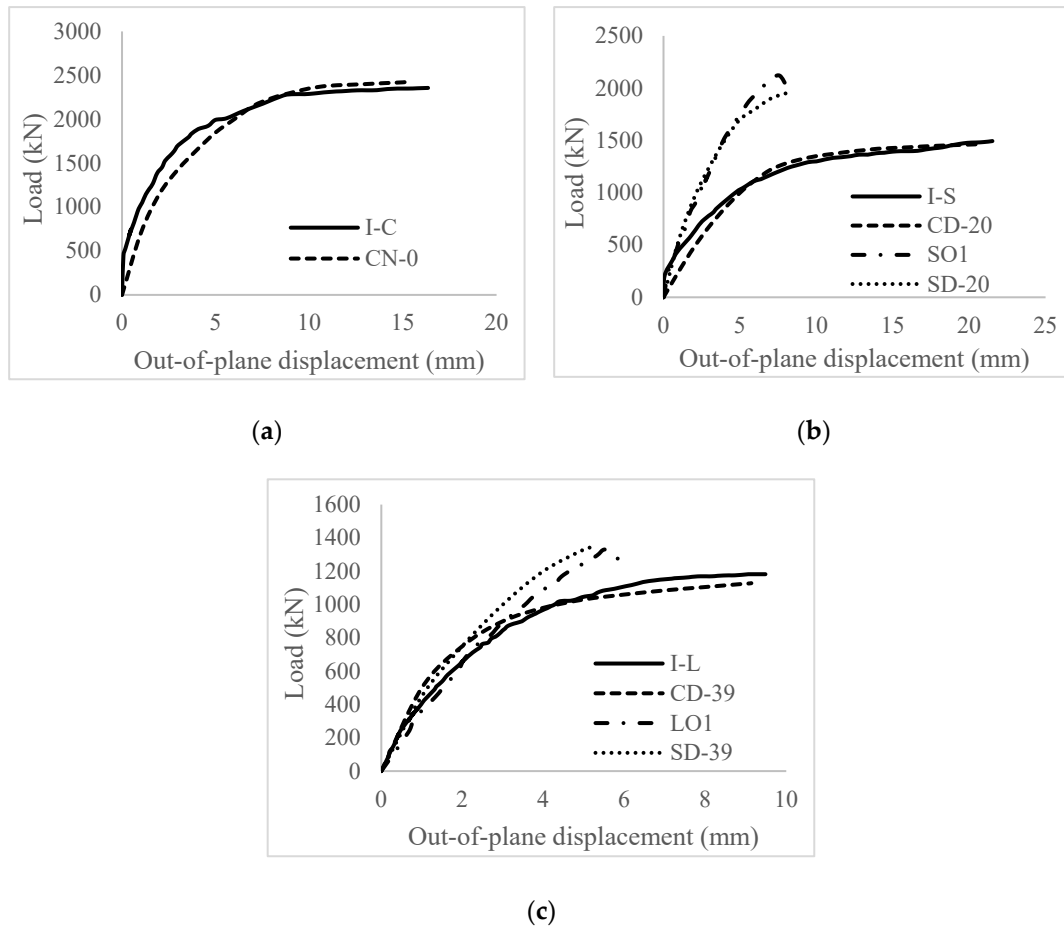


Figure 7. Load versus out-of-plane displacement curves of FEA models and test specimens with: (a) no opening; (b) small openings; (c) large openings.

In general, the use of TRM enhanced the stiffness and reduced the out-of-plane deformation capacity of walls with openings. The stiffness improvement could be attributed to the increase in the cross-sectional area of the walls and the additional tensile reinforcement provided by the TRM sheets.

Failure of Control and Strengthened Wall Models

The maximum compressive principal strain values and distributions in concrete indicate the failure type and its location, respectively. All control and strengthened wall models failed due to concrete crushing, as shown in Figure 8. The failure in the control models with openings (CD-20 and CD-39) was along the diagonal wall lines at the top corners of the walls and openings. In these models, the concrete was crushed, and the vertical steel bars buckled due to the high compressive stresses resulting from the eccentric axial load. Figure 8a,b show the maximum principal strain distribution at the corner of the opening in the control models. For the strengthened walls (SD-20 and SD-39), the failure took place at

the bottom of the piers (Figure 8c,d). Although there were high compressive strains along the diagonal between the wall and opening corners, the reduction in the concrete volume due to the openings led to higher axial compressive forces resulting in higher compressive strains at the bottom of the piers.

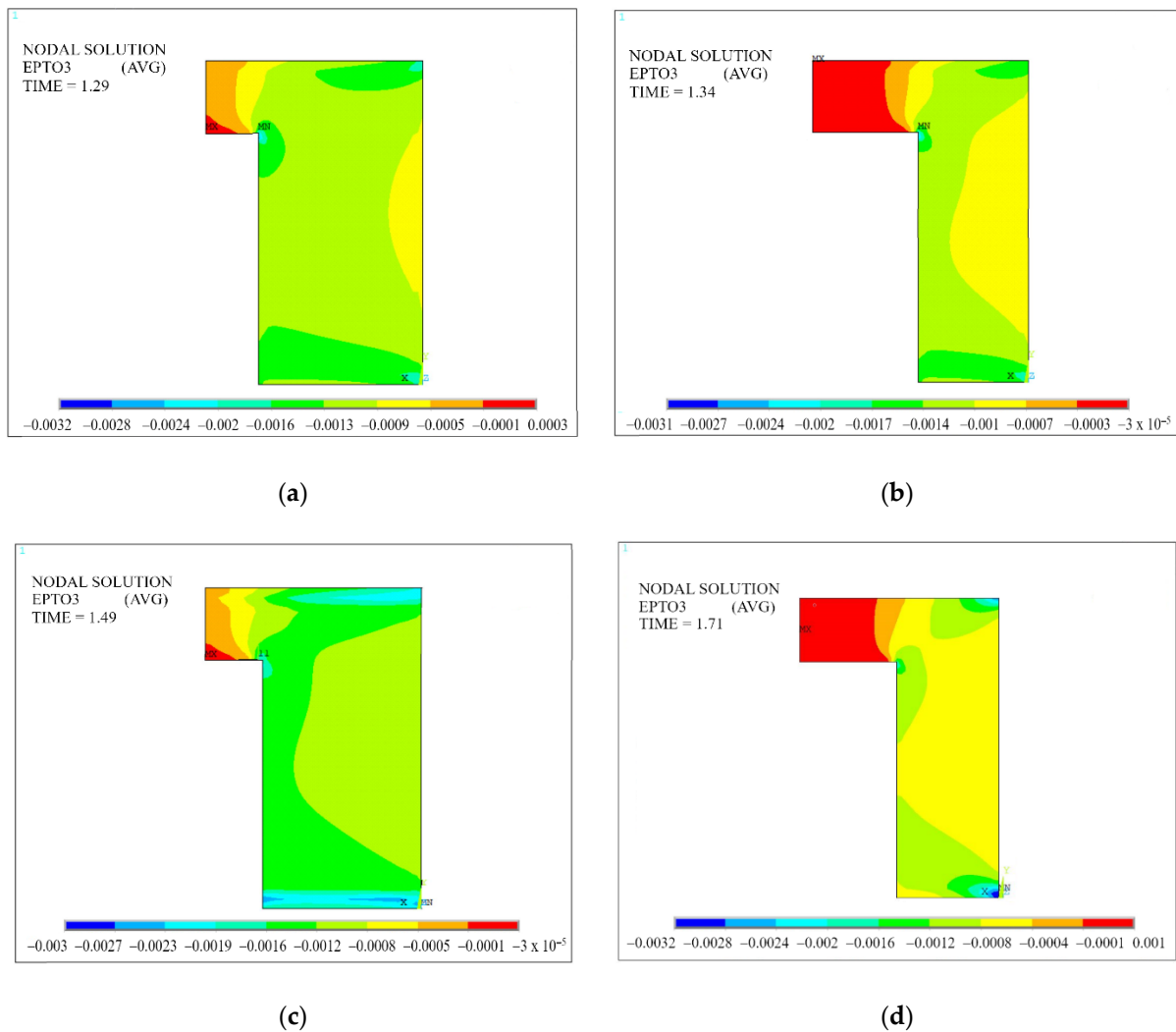


Figure 8. Concrete principal strain distribution: (a) CD-20; (b) CD-39; (c) SD-20; (d) SD-39.

5. Parametric Study Results

After the validation of the FEA models, a parametric study was carried out to explore the contribution of TRM in strengthening RC walls considering various opening sizes, types, numbers and orientations of window openings, and TRM strengthening configurations. Figure 9 shows the geometry and configurations of the walls' openings considered in the parametric study where the subscripts W and O stand for wall and opening, respectively.

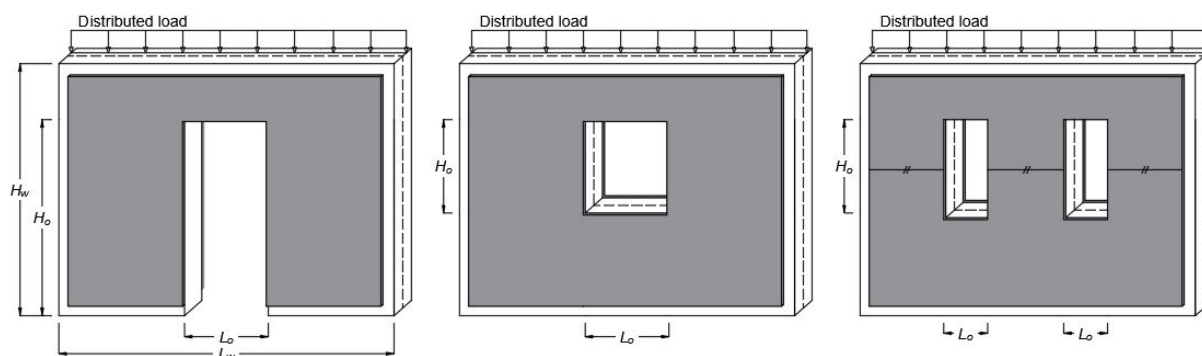


Figure 9. Geometry of the wall models with various opening types and configurations.

5.1. Effect of Opening Size

Eight FEA wall models with door-type openings of four different lengths in as built and TRM-strengthened RC walls were developed to study the impact of various opening sizes (Figure 9a). The spandrel height (above the opening) was constant for all models. The results of the walls, including the five validated models, are presented in Table 3.

Table 3. Results of wall models with various opening sizes.

Model ID	L_o (mm)	H_o (mm)	A_o/A_w (%)	N_u (kN)	$(\frac{N_u - N_{u,CN-0}}{N_{u,CN-0}})$ (%)	$(\frac{N_u - N_{u,control}}{N_{u,control}})$ (%)	Failure Mode
CN-0	-	-		2423	0		RB and CC at wall corners
CD-20	450	1050	20	1464	-40		CC along the diagonal line
SD-20	450	1050	20	1967	-18	35	CC at bottom of wall pier
CD-26	600	1050	26	1419	-41		CC along the diagonal line
SD-26	600	1050	26	1829	-25	29	CC at bottom of wall pier
CD-30	700	1050	30	1301	-46		CC along the diagonal line
SD-30	700	1050	30	1639	-32	26	CC at bottom of wall pier
CD-35	800	1050	35	1176	-52		CC along the diagonal line
SD-35	800	1050	35	1442	-41	23	CC at bottom of wall pier
CD-39	900	1050	39	1128	-53		CC along the diagonal line
SD-39	900	1050	39	1345	-45	19	CC at bottom wall corner
CD-45	1050	1050	45	911	-62		CC at bottom wall corner
SD-45	1050	1050	45	1056	-56	16	CC at bottom wall corner

Note: L_o = the length of the opening, H_o = the height of the opening, A_o = the area of the opening, A_w = the area of the wall, N_u = the axial capacity, $N_{u,CN-0}$ = the axial capacity of the solid wall, $N_{u,control}$ = the axial capacity of the corresponding control model, RB = Buckling of the reinforcement, CC = concrete crushing.

All wall panels (control and strengthened) were not able to restore the axial capacity of the solid wall (see Table 3). The enhancements in the axial strength of SD-20, SD-26, SD-30, SD-35, SD-39, and SD-45 were 34.4, 30.2, 26.0, 22.6, 19.2, and 16.8%, respectively, when compared to the corresponding control models. Moreover, when the opening area ratio was increased from 20% to 45%, the TRM contribution dropped by approximately 51%. As a result, the axial strength improvement was higher in models with smaller opening sizes, demonstrating that the effectiveness of TRM was dominant when the opening was smaller. This could be attributed to the higher piers' cross-sections aspect ratios in the walls with a smaller door opening, resulting in more ductile behavior and higher reinforcement contribution. In addition, more even compressive strain distribution was observed at the bottom of the piers in walls with a smaller door opening at failure. Similar results were observed by Popescu et al. [12] with the use of FRP instead of TRM.

Although strengthening the wall with TRM improved the axial strength of the walls, the failure mode remained unchanged. All models failed by concrete crushing. The crushing in the control models was along the diagonal line between the top corners of the opening and the wall, except for CD-45 where the highest compressive stresses were

observed at the bottom of the piers. This is due to the decrease in the cross-sectional area resulting in higher compression stresses. For the strengthened models, the crushing of the concrete took place at the bottom of the piers near the opening. Therefore, strengthening the walls with TRM did not impact the failure mechanism but shifted the location of the concrete crushing.

The principal compressive strain distributions in the concrete for the control and strengthened models with 45% opening area ratio are shown in Figure 10. The maximum strains in the control and strengthened models (CD-45 and SD-45) were at the bottom of the piers. When compared to the control model with an opening area ratio of 20% (Figure 8a), the maximum strains in model CD-20 were shifted from the top corner of the opening to the bottom of the piers in CD-45. For the strengthened models, the maximum strains in models SD-20 (Figure 8c) and SD-45 (Figure 10b) were at the bottom of the piers. However, these compressive strains were more uniformly distributed in model SD-20 specifying that the failure was more ductile than SD-45.

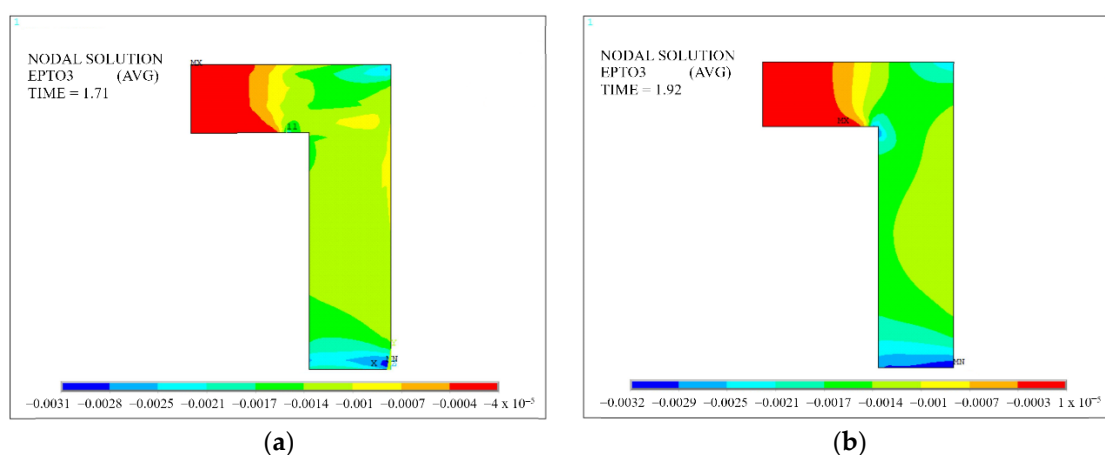


Figure 10. Concrete principal strain distribution: (a) CD-45; (b) SD-45.

5.2. Effect of Opening Type

Two FEA wall models having window openings with a surface area ratio (A_o/A_w) of 20% were developed and compared with the corresponding walls with doors to study the opening-type effect (Figure 9a,b). The axial load capacities of the walls and the TRM effectiveness are presented in Table 4, where W stands for type of window opening.

Table 4. Results of wall models with various opening types.

Model ID	Type of Opening	L_o (mm)	H_o (mm)	A_o/A_w (%)	N_u (kN)	$(\frac{N_u - N_{u,CN-0}}{N_{u,CN-0}})$ (%)	$(\frac{N_u - N_{u,control}}{N_{u,control}})$ (%)	Failure Mode
CN-0	None	-	-	-	2423	0.0		RB and CC at wall corners
CD-20	Door	450	1050	20	1464	-40		CC along the diagonal line
SD-20	Door	450	1050	20	1967	-19	34	CC at bottom of wall pier
CW-20	Window	900	525	20	1696	-30		CC at top wall corner
SW-20	Window	900	525	20	2141	-12	26	CC at top wall corner

The control models CD-20 and CW-20 reached an ultimate load of 1464 and 1696 kN, respectively, resulting in 40% and 30% reduction in the axial strength as compared to the solid model (CN-0). On the other hand, for the strengthened wall models, the increase in the axial strength of SD-20 and SW-20 were 34% and 26%, respectively, as compared to the corresponding control ones. As a result, the models with window openings had higher axial strength as compared to the ones with door openings. However, the TRM effectiveness was higher in models with door openings.

The mode of failure remained unchanged (concrete crushing) regardless of the opening type. However, the location of the failure was shifted from the bottom of the piers to the

top corner of the wall when the door opening was replaced with a window. The additional concrete below the window opening strengthened the lower part of the wall and, thus, shifted the failure to the upper part.

5.3. Effect of Window Opening Configuration

A total of ten FEA wall models with window-type openings of various configurations (numbers and orientations) were developed (Figure 9b,c). The results of the walls are presented in Table 5, where the first number identifies the number of openings, and the last three digits represent the opening length (L_o).

Table 5. Results of wall models with various opening configurations.

Model ID	No. of Openings	L_o (mm)	H_o (mm)	A_o/A_w (%)	N_u (kN)	$(\frac{N_u - N_{u,CN-0}}{N_{u,CN-0}})$ (%)	$(\frac{N_u - N_{u,control}}{N_{u,control}})$ (%)	Failure Mode
CN-0	0	-	-	-	2423	0	-	RB and CC at wall corners
CW1-10-450	1	450	525	10	1758	-27	-	CC at top wall corner
SW1-10-450	1	450	525	10	2249	-7	28	CC at top wall corner
CW1-10-525	1	525	450	10	1669	-31	-	CC at top wall corner
SW1-10-525	1	525	450	10	2284	-11	37	CC at top wall corner
CW2-10-225	2	225	525	10	1804	-26	-	CC at top wall corner
SW2-10-225	2	225	525	10	2534	5	41	CC at top wall corner
CW1-20-900	1	900	525	20	1696	-30	-	CC at opening corner
SW1-20-900	1	900	525	20	2141	-12	26	CC at opening corner
CW1-20-525	1	525	900	20	1364	-44	-	CC at opening corner
SW1-20-525	1	525	900	20	1632	-33	20	CC at opening corner
CW2-20-450	2	450	525	20	1779	-27	-	CC at top wall corner
SW2-20-450	2	450	525	20	2297	-5	29	CC at top wall corner

For walls with the smaller opening area ratio (10%), all models (control and strengthened) were not able to restore the axial capacity of the solid wall except SW2-10-225 (Table 5). Furthermore, the control model with two openings outperformed the walls with only one in terms of axial load capacity. This could be attributed to the load being distributed over three piers rather than two. For the strengthened walls, the highest axial strength improvements were in models with two openings. Moreover, the improvement in the axial capacities of SW1-10-450 and SW1-10-525 were 28% and 37%, respectively, as compared to their corresponding control models indicating that the effectiveness of TRM was more dominant when the aspect ratio of the opening (H_o/L_o) is lower. In addition, models CW1-10-450 and CW2-20-450 had equivalent axial strengths suggesting that using two openings was equivalent to decreasing the opening area ratio by 50%.

The failure mode of all walls was concrete crushing. Although the opening configuration had no impact on the failure mechanism, the location of the failure varied. The crushing of the concrete started at the corners of the walls in all models except for CW1-20-900, SW1-20-900, CW1-20-525, and SW1-20-525, where the failure occurred at the opening's corners.

The walls with opening-to-wall area ratio of 20%, which had the lowest axial strengths, were selected for comparison of concrete compressive strains (Figure 11). High strain intensity was observed along the diagonal line between the top corner of the wall and the top corner of the opening in all models. However, the highest strain values in the control models were at the top corner of the opening, while the maximum strains were at the wall's top corner for the strengthened walls. Furthermore, large strain values were developed in the middle pier and were distributed horizontally between the two openings in CW2-20-450 and SW2-20-450. Since all models failed due to concrete crushing, it can be concluded that the location of the failure depends mainly on the location and orientation of the openings. Thus, proper strengthening configuration should be applied based on the location of the failure.

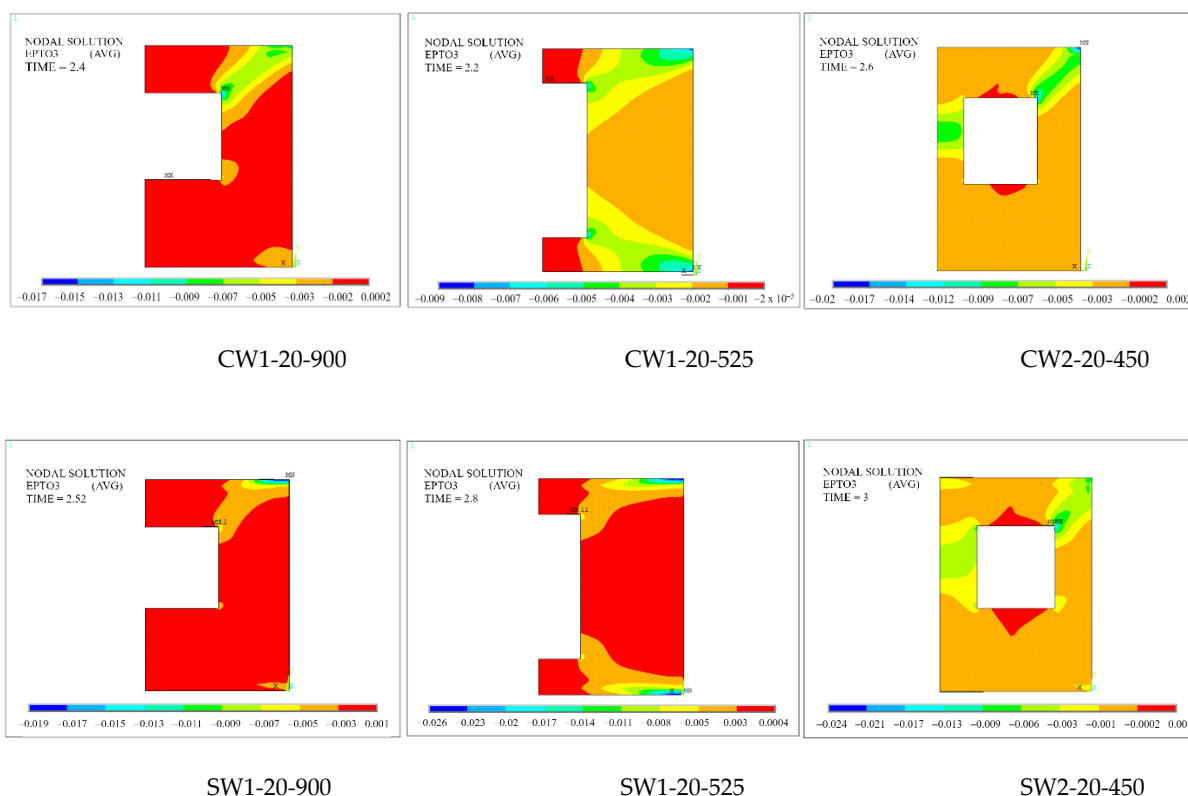


Figure 11. Concrete compressive strains in walls with window opening area ratio of 20%.

5.4. Effect of TRM Configuration

To investigate the effect of various TRM strengthening configurations, the two validated control walls (CD-20 and CD-39) were retrofitted with two different TRM arrangements (strips applied around the opening and U-shaped jackets). The strips around the opening were configured based on the observed concrete crushing at the opening corners of the control walls as reported by the experimental study [3] and used for validation of the FEA wall models. On the other hand, the U-shaped TRM jackets were employed in the FEA wall models to mitigate or delay the concrete crushing at the bottom of the piers, which was observed in the strengthened test specimens [19]. For simplicity, a perfect bond between the mortar and concrete was assumed near the top and side supports to simulate the confinement action in the presence of anchorage in real application. Figure 12 shows the TRM strengthening configurations adopted in this study. The results of the walls are presented in Table 6, where the last letters refer to the strengthening configuration (SH for sheets, ST for strips, U for U-shaped jackets).

Table 6. Results of wall models with various strengthening configurations.

Model ID	Strengthening Configuration	A_o/A_w (%)	N_u (kN)	Difference (%)	Failure Mode
CD-20	-	20	1464		CC along the diagonal line
SD-20SH	Sheets	20	1967	34	CC at bottom of wall pier
SD-20ST	Strips	20	1878	28	CC at bottom of wall pier
SD-20U	U-shaped	20	2213	51	CC at opening corner
CD-39	-	39	1128		CC along the diagonal line
SD-39SH	Sheets	39	1345	19	CC at bottom of wall pier
SD-39ST	Strips	39	1288	14	CC at bottom of wall pier
SD-39U	U-shaped	39	1566	39	CC at bottom of wall pier

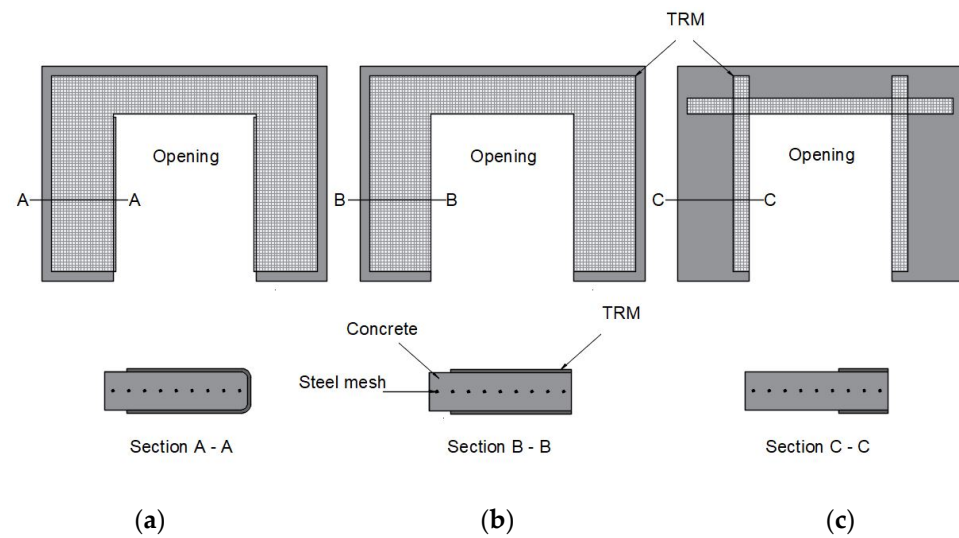


Figure 12. TRM strengthening configurations: (a) U-shaped jackets; (b) sheets; (c) strips.

The axial capacity of the strengthened models was enhanced as compared to their corresponding control models (Table 6). The ultimate loads of models with an opening area ratio of 20% (SD-20SH, SD-20ST, and SD-20U) were 1967, 1878, and 2213 kN, respectively, with 34.4, 28.3, and 51.2% improvement in the axial strength when compared with C-20. On the other hand, models SD-39SH, SD-39ST, and SD-39U failed at 1345, 1288, and 1566 kN, respectively, resulting in 19, 14, and 39% enhancement in the axial load capacity. Furthermore, the rise in the axial resistance of models SD-20U and SD-39U was 13% and 17%, respectively, as compared to models SD-20SH and SD-39SH. The decrease in the pier's cross-section aspect ratio in SD-39U resulted in slightly higher TRM confinement effectiveness when compared to SD-20U.

Although a good level of confinement is hard to achieve due to the high aspect ratio of the piers' cross-sections, the U-shaped TRM jacket was the most effective configuration in improving the axial strength regardless of the opening size.

All models failed due to crushing of the concrete on the compression side of the walls, indicating that the failure mode is independent of the strengthening configurations. However, the location of the failure was different. For the strengthened walls, the crushing happened at the bottom corner of the piers for all models except SD-20U and SD-39U, where the failure occurred at the opening corner. Confining the walls shifted the compressive strains from the bottom of the piers to the opening corner. Furthermore, the strains in the textile never reached the ultimate level. In fact, the maximum tensile strain values were approximately 10% of the ultimate value ($\epsilon_f = 0.018$), suggesting that the increase in the axial capacities of the walls may be attributed to the mortar by increasing the cross-sectional area of the models. In addition, the use of U-shaped TRM jackets allowed the steel mesh to reach yielding, ensuring ductile behavior of the walls.

6. Comparison of FEA and Theoretical Results

The axial load capacities of the control and strengthened FEA wall models were compared with existing empirical solutions considering various opening numbers, sizes, and orientations. Among many empirical models presented in the literature, the model proposed by Guan et al. [37] was selected to account for the effect of the openings' lengths and heights on the axial strength of walls under two-way action. The axial load capacity of the control walls with openings can be obtained using Equation (13) as follows:

$$N_{uo} = (k_1 - k_2\alpha_{xy})N_u \quad (13)$$

where k_1 and k_2 are coefficients specified by performing regression analysis, α_{xy} is a dimensionless parameter accounting for the effect of the opening's height and length, and N_u

is the axial strength of the corresponding solid wall (i.e., identical wall dimensions with no openings). The axial strength of the solid wall (N_u) was calculated according to the semiempirical equation, Equation (14), introduced by Doh and Fragomeni [1]:

$$N_u = 2f'_c{}^{0.7}(t - 1.2e - 2e_a)L_w \quad (14)$$

where f'_c is the compressive strength of the concrete, t is the thickness of the wall, and e and e_a are the eccentricities that account for the first and second order effects, respectively. The details of these models, including the calculations of the parameters involved, are discussed in Sabau et al. [19] and Guan et al. [37].

The axial load capacities of the strengthened models were also obtained using Equation (13). However, the total thickness of the wall including the TRM sheets was considered since all control and strengthened wall models failed due to concrete crushing. It is noted that the effect of steel reinforcement is insignificant when one layer of steel mesh is placed in the center of the wall's cross-section [38]. Hence, the effect of the steel reinforcement was neglected. The results of the FEA and analytical solutions are shown in Table 7.

Table 7. Results of FEA and theoretical axial load capacities.

Model ID	No. of Openings	L_o (mm)	H_o (mm)	A_o/A_w (%)	α_{xy}	$N_{uo, FEA}$ (kN)	$N_{uo, theoretical}$ (kN)	Difference (%)
CN-0	0	-	-	-	-	2423	2324	4
CD-20	1	450	1050	20	0.44	1464	1321	11
SD-20	1	450	1050	20	0.44	1967	2375	17
CD-26	1	600	1050	26	0.45	1419	1279	11
SD-26	1	600	1050	26	0.45	1829	2300	20
CD-30	1	700	1050	30	0.48	1301	1154	13
SD-30	1	700	1050	30	0.48	1639	2075	21
CD-35	1	800	1050	35	0.50	1176	1070	10
SD-35	1	800	1050	35	0.50	1442	1825	21
CD-39	1	900	1050	39	0.53	1128	966	17
SD-39	1	900	1050	39	0.53	1345	1707	21
CD-45	1	1050	1050	45	0.57	911	798	14
SD-45	1	1050	1050	45	0.57	1056	1345	21
CW1-10-450	1	450	525	10	0.37	1758	1633	8
SW1-10-450	1	450	525	10	0.37	2249	2838	21
CW1-10-525	1	525	450	10	0.38	1669	1571	6
SW1-10-525	1	525	450	10	0.38	2284	2825	19
CW2-10-225	2	225	525	10	0.34	1804	1738	4
SW2-10-225	2	225	525	10	0.34	2534	3126	19
CW1-20-900	1	900	525	20	0.40	1696	1487	14
SW1-20-900	1	900	525	20	0.40	2141	2675	20
CW1-20-525	1	525	900	20	0.47	1364	1195	14
SW1-20-525	1	525	900	20	0.47	1632	2050	20
CW2-20-450	2	450	525	20	0.37	1779	1621	10
SW2-20-450	2	450	525	20	0.37	2297	2915	21
Avg								15

The average difference in the axial load capacity of all models was approximately 15%. The strengthened models had higher discrepancies as compared to the corresponding control walls. However, the axial load capacities of the strengthened walls yielded reasonable correlation with the theoretical predictions with an average difference of 19%. This indicates that the contribution of the TRM was mainly due to the geometrical changes of the wall's cross-section. Thus, the TRM contribution was mostly based on the mortar rather than the textiles. Figure 13 shows a scatter plot of the theoretical and FEA results, which indicates good agreement of the axial strength predictions.

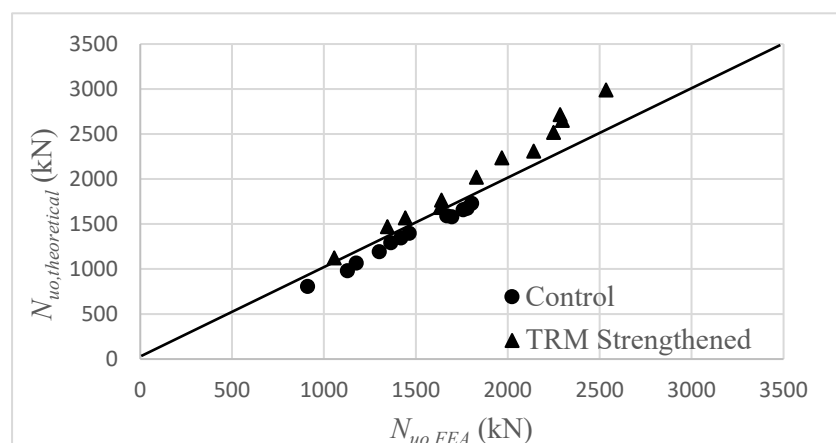


Figure 13. Comparison of FEA and theoretical axial load capacities.

As a result, the effect of the mortars' compressive and tensile strengths and TRM thickness need to be investigated. In addition, a detailed analytical and/or empirical solutions should be developed to optimize the design of TRM-strengthened walls with cutout openings.

7. Conclusions

In the present study, FEA models of TRM strengthening RC walls were developed and validated with an experimental study from the literature. Subsequently, a parametric study was carried out to explore the contribution of TRM in strengthening RC walls considering various opening sizes, types, numbers and orientations, and strengthening configurations. The primary conclusions were as follows:

- Strengthening RC walls with openings enhanced their axial strength. This improvement was observed more frequently in models with smaller opening sizes, demonstrating that the effectiveness of TRM was more dominant when the wall's axial capacity was higher. Furthermore, all models failed by concrete crushing regardless of the opening size; however, the location of the failure varied. The crushing of the concrete in the control models was along the diagonal line between the top corners of the opening and the wall except for CD-45, where the highest compressive stresses were observed at the bottom of the piers. For the strengthened models, the failure took place at the bottom of the piers near the opening.
- The models with window openings outperformed the ones with door openings. However, the effectiveness of TRM was more dominant in walls with door-type openings.
- The opening configuration showed a significant effect on the axial capacity where the highest was achieved in walls with two openings. Model SW2-10-225 was the only model that was able to restore the axial capacity of the solid wall. Furthermore, the effectiveness of TRM was dominant when the aspect ratio of the opening (H_o/L_o) was lower.
- Confining the piers with U-shaped TRM jackets was the most effective configuration in improving the walls' axial strengths with maximum enhancements of 16 and 22% as compared to the models strengthened with side-bonded sheets and strips, respectively. Moreover, TRM confinement was able to shift the failure from the bottom of the piers to the top part of the wall near the opening's corners.
- The axial strength predictions of the FEA and existing empirical models were in good agreement with average discrepancy of 15%. In the case of strengthened models, the FEA results yielded reasonable correlation with the theoretical predictions with an average difference of 19%. This indicates that the contribution of the TRM was mainly due to the geometrical changes of the wall's cross-section since the theoretical models used were proposed for control walls.

The FEA models in this study may be used in the future to further investigate the effect of several parameters such as mortar strengths and TRM thickness on the axial strength of RC walls and to develop design guidelines for more sustainable structures.

Author Contributions: Data curation, M.A.; investigation, M.A. and A.P.; conceptualization, A.P.; methodology, M.A. and A.P.; project administration, A.P.; software, M.A.; validation, M.A., supervision, A.P.; writing—original draft, M.A.; writing—review and editing, A.P. All authors have read and agreed to the published version of the manuscript.

Funding: This research received no external funding.

Data Availability Statement: Not applicable.

Conflicts of Interest: The authors declare no conflict of interest.

References

1. Doh, J.H.; Fragomeni, S. Evaluation of experimental work on concrete walls in one and two-way action. *Aust. J. Struct. Eng.* **2005**, *6*, 37–52. [[CrossRef](#)]
2. Fragomeni, S.; Doh, J.H.; Lee, D.J. Behavior of axially loaded concrete wall panels with openings: An experimental study. *Adv. Struct. Eng.* **2012**, *15*, 1345–1358. [[CrossRef](#)]
3. Popescu, C.; Sas, G.; Sabau, C.; Blanksvärd, T. Effect of cut-out openings on the axial strength of concrete walls. *J. Struct. Eng.* **2016**, *142*, 04016100. [[CrossRef](#)]
4. Sabau, C.; Popescu, C.; Bagge, N.; Sas, G.; Blanksvärd, T.; Täljsten, B. Local and global behavior of walls with cut-out openings in multi-story reinforced concrete buildings. *Eng. Struct.* **2019**, *187*, 57–72. [[CrossRef](#)]
5. Valeri, P.; Guaita, P.; Baur, R.; Ruiz, M.F.; Fernández-Ordóñez, D.; Muttoni, A. Textile reinforced concrete for sustainable structures: Future perspectives and application to a prototype pavilion. *Struct. Concr.* **2020**, *21*, 2251–2267. [[CrossRef](#)]
6. Assefa, G.; Ambler, C. To demolish or not to demolish: Life cycle consideration of repurposing buildings. *Sustain. Cities Soc.* **2017**, *28*, 146–153. [[CrossRef](#)]
7. Triantafyllou, T.; Papanicolaou, C. Shear strengthening of reinforced concrete members with textile reinforced mortar (TRM) jackets. *Mater. Struct.* **2006**, *39*, 93–103. [[CrossRef](#)]
8. Gonzalez, J.; Faleschini, F.; D’Antino, T.; Pellegrino, C. Bond behaviour and sustainability of fibre reinforced cementitious matrix composites applied to masonry elements. In Proceedings of the Fifteenth International Conference on Civil, Structural and Environmental Engineering Computing, Prague, Czech Republic, 1–4 September 2015.
9. Koutas, L.N.; Tetta, Z.; Bournas, D.A.; Triantafyllou, T.C. Strengthening of concrete structures with textile reinforced mortars: State-of-the-art review. *J. Compos. Constr.* **2019**, *23*, 03118001. [[CrossRef](#)]
10. Mohammed, B.S.; Ean, L.W.; Malek, M.A. One way RC wall panels with openings strengthened with CFRP. *Constr. Build. Mater.* **2013**, *40*, 575–583. [[CrossRef](#)]
11. Lima, M.M.; Doh, J.-H.; Hadi, M.N.S. Experimental study on RC walls with opening strengthened by externally bonded CFRP. *J. Compos. Constr.* **2019**, *23*, 04019008. [[CrossRef](#)]
12. Popescu, C.; Sas, G.; Blanksvärd, T.; Täljsten, B. Concrete walls with cutout openings strengthened by FRP confinement. *J. Compos. Constr.* **2017**, *21*, 04016106. [[CrossRef](#)]
13. Ombres, L. Flexural analysis of reinforced concrete beams strengthened with a cement based high strength composite material. *Compos. Struct.* **2011**, *94*, 143–155. [[CrossRef](#)]
14. Bournas, D.A.; Triantafyllou, T.C. Bar buckling in RC columns confined with composite materials. *J. Compos. Constr.* **2011**, *15*, 393–403. [[CrossRef](#)]
15. Colajanni, P.; De Domenico, F.; Recupero, A.; Spinella, N. Concrete columns confined with fibre reinforced cementitious mortars: Experimentation and modeling. *Constr. Build. Mater.* **2014**, *52*, 375–384. [[CrossRef](#)]
16. Parvin, A.; Alhusban, M. Lateral deformation capacity and plastic hinge length of RC columns confined with textile reinforced mortar jackets. *Civil. Eng.* **2021**, *2*, 670–691. [[CrossRef](#)]
17. Parvin, A.; Alhusban, M. Finite-element analysis of textile-reinforced mortar strengthening of shear-deficient reinforced concrete beams. *J. Compos. Constr.* **2022**, *26*, 04022037. [[CrossRef](#)]
18. Todut, C.; Dan, D.; Stoian, V. Numerical and experimental investigation on seismically damaged reinforced concrete wall panels retrofitted with FRP composites. *Comp. Struct.* **2015**, *119*, 648–665. [[CrossRef](#)]
19. Sabau, C.; Popescu, C.; Sas, G.; Blanksvärd, T.; Täljsten, B. Axially loaded RC walls with cutout openings strengthened with FRCM composites. *J. Compos. Constr.* **2018**, *22*, 04018046. [[CrossRef](#)]
20. Portal, N.W.; Lundgren, K.; Wallbaum, H.; Malaga, K. Sustainable potential of textile-reinforced concrete. *J. Mater. Civ. Eng.* **2015**, *27*, 04014207. [[CrossRef](#)]
21. Ismail, N.; Ingham, J.M. In-plane and out-of-plane testing of unreinforced masonry walls strengthened using polymer textile reinforced mortar. *Eng. Struct.* **2016**, *118*, 167–177. [[CrossRef](#)]

22. Koutas, L.; Bousias, S.N.; Triantafillou, T.C. Seismic strengthening of masonry-infilled RC frames with TRM: Experimental study. *J. Compos. Constr.* **2015**, *19*, 04014048. [[CrossRef](#)]
23. Triantafillou, T.C.; Karlos, K.; Kapsalis, P.; Georgiou, L. Innovative structural and energy retrofitting system for masonry walls using textile reinforced mortars combined with thermal insulation: In-plane mechanical behavior. *J. Compos. Constr.* **2018**, *22*, 04018029. [[CrossRef](#)]
24. Koutas, L.; Bournas, D.A. Out-of-plane strengthening of masonry-infilled RC frames with textile-reinforced mortar jackets. *J. Compos. Constr.* **2019**, *23*, 04018079. [[CrossRef](#)]
25. ANSYS®. *Academic Research Mechanical Release 18*; Help System; ANSYS, Inc.: Canonsburg, PA, USA, 2018. Available online: <http://www.ansys.com/> (accessed on 25 January 2022).
26. Bazant, Z.P.; Gambarova, P.G. Crack shear in concrete: Crack band microplane model. *J. Struct. Engr.* **1984**, *110*, 2015–2036. [[CrossRef](#)]
27. Bazant, Z.P.; Oh, B.H. Microplane model for progressive fracture of concrete and rock. *J. Engr. Mech.* **1985**, *111*, 559–582. [[CrossRef](#)]
28. Zreid, I.; Kaliske, M. A gradient enhanced plasticity-damage microplane model for concrete. *Comp. Mech.* **2018**, *62*, 1239–1257. [[CrossRef](#)]
29. ACI 318; Building Code Requirements for Structural Concrete (ACI 318–19) and Commentary (ACI 318R–19). American Concrete Institute (ACI): Farmington Hills, MI, USA, 2019.
30. Jiang, H.; Zhao, J. Calibration of the continuous surface cap model for concrete. *Finite Elem. Anal. Des.* **2015**, *97*, 1–19. [[CrossRef](#)]
31. Hognestad, E. *A Study of Combined Bending and Axial Load in Reinforced Concrete Members*; Urbana Champaign: Urbana, IL, USA, 1951.
32. Desayi, P.; Krishnan, S. Equation for the stress-strain curve of concrete. *J. Proc.* **1964**, *61*, 345–350. [[CrossRef](#)]
33. Alhaddad, M.; Siddiqui, N.; Abadel, A.; Alsayed, S.; Al-salloum, Y. Numerical investigations on the seismic behavior of FRP and TRM upgraded RC exterior beam-column joints. *J. Compos. Constr.* **2012**, *16*, 308–321. [[CrossRef](#)]
34. Younis, A.; Ebead, U. Bond characteristics of different FRCM systems. *Constr. Build. Mater.* **2018**, *175*, 610–620. [[CrossRef](#)]
35. Omran, H.Y.; El-Hacha, R. Nonlinear 3D finite element modeling of RC beams strengthened with prestressed NSM-CFRP strips. *Constr. Build. Mater.* **2012**, *31*, 74–85. [[CrossRef](#)]
36. Ombres, L. Analysis of the bond between fabric reinforced cementitious mortar (FRCM) strengthening systems and concrete. *Compos. B Eng.* **2015**, *69*, 418–426. [[CrossRef](#)]
37. Guan, H.; Cooper, C.; Lee, D.-J. Ultimate strength analysis of normal and high strength concrete wall panels with varying opening configurations. *Eng. Struct.* **2010**, *32*, 1341–1355. [[CrossRef](#)]
38. Fragomeni, S. Design of Normal and High Strength Reinforced Concrete Walls. Ph.D. Thesis, University of Melbourne, Melbourne, Australia, 1995.